

HIGH-RESOLUTION SPECTROSCOPY OF EXTREMELY METAL-POOR STARS FROM SDSS/SEGUE. III.
UNEVOLVED STARS WITH $[\text{Fe}/\text{H}] \lesssim -3.5$ *

TADAFUMI MATSUNO,^{1,2} WAKO AOKI,^{2,1} TIMOTHY C. BEERS,³ YOUNG SUN LEE,⁴ AND SATOSHI HONDA⁵

¹*Department of Astronomical Science, School of Physical Sciences, SOKENDAI (The Graduate University for Advanced Studies), 2-21-1 Osawa, Mitaka, Tokyo 181-8588, Japan*

²*National Astronomical Observatory of Japan (NAOJ), 2-21-1 Osawa, Mitaka, Tokyo 181-8588, Japan*

³*Department of Physics and JINA Center for the Evolution of the Elements, University of Notre Dame, Notre Dame, IN 46556, USA*

⁴*Department of Astronomy and Space Science, Chungnam National University, Daejeon 34134, Korea*

⁵*Nishi-Harima Astronomical Observatory, Center for Astronomy, University of Hyogo, 407-2 Nishigaichi, Sayo-cho, Sayo, Hyogo 679-5313, Japan*

ABSTRACT

We present elemental abundances for eight unevolved extremely metal-poor stars with $T_{\text{eff}} > 5500$ K, among which seven have $[\text{Fe}/\text{H}] < -3.5$. The sample is selected from the Sloan Digital Sky Survey / Sloan Extension for Galactic Understanding and Exploration (SDSS/SEGUE), and our previous high-resolution spectroscopic follow-up with the Subaru Telescope (Aoki et al.). Several methods to derive stellar parameters are compared, and no significant offset in the derived parameters is found in most cases. From an abundance analysis relative to the standard extremely metal-poor star G 64–12, an average Li abundance for stars with $[\text{Fe}/\text{H}] < -3.5$ is $A(\text{Li}) = 1.90$, with a standard deviation of $\sigma = 0.10$ dex. This result confirms that lower Li abundances are found at lower metallicity, as suggested by previous studies, and demonstrates that the star-to-star scatter is small. The small observed scatter could be a strong constraint on Li-depletion mechanisms proposed for explaining the low Li abundance at lower metallicity. Our analysis for other elements obtained the following results: i) A statistically significant scatter in $[X/\text{Fe}]$ for Na, Mg, Cr, Ti, Sr, and Ba, and an apparent bimodality in $[\text{Na}/\text{Fe}]$ with a separation of ~ 0.8 dex, ii) an absence of a sharp drop in the metallicity distribution, and iii) the existence of a CEMP-*s* star at $[\text{Fe}/\text{H}] \simeq -3.6$ and possibly at $[\text{Fe}/\text{H}] \simeq -4.0$, which may provide a constraint on the mixing efficiency of unevolved stars during their main-sequence phase.

arXiv:1706.04712v1 [astro-ph.SR] 15 Jun 2017

1. INTRODUCTION

Extremely metal-poor (EMP; $[\text{Fe}/\text{H}] < -3.0$) stars provide chemical information on the Universe at a unique phase of its evolution. Precise cosmic microwave background (CMB) measurements from space constrain the conditions at the time of the Big Bang (e.g., [Planck Collaboration et al. 2016](#)), whereas observations of galaxies across a wide range of redshift trace galaxy evolution over cosmic time (e.g., [Madau & Dickinson 2014](#)). However, in order to connect galaxy formation with the Big Bang, understanding of the formation and evolution of first-generation stars is indispensable. Since the chemical abundances of EMP stars are not generally affected by nucleosynthesis processes other than the Big Bang and the supernovae explosions of the first stars, they can fill the gap between observations of the CMB and those of later-forming galaxies.

Stellar Li abundances deliver uniquely important information, since Li is the only element (beyond H and He) that is synthesized in the Big Bang to a significant degree and can be measured in the atmospheres of many EMP stars. Although the constant Li abundance found in metal-poor turn-off stars was formerly regarded as a constraint on Big Bang nucleosynthesis ([Spite & Spite 1982a,b](#)), the “Li plateau” value turned out to stand in contradiction to the Li abundance predicted by Big Bang nucleosynthesis models based on the recent CMB observations ([Coc et al. 2004](#); [Cyburt et al. 2016](#)). Theoretical trials invoking Li-depletion mechanisms in the formation and evolution of low-mass metal-poor stars have attempted to explain this discrepancy (e.g., [Richard et al. 2005](#); [Piau et al. 2006](#); [Fu et al. 2015](#)). One difficulty is reproducing the small observed scatter in Li abundances for metal-poor turn-off stars with $-2.5 \lesssim [\text{Fe}/\text{H}] \lesssim -1.6$. In addition, recent observations demonstrate that the plateau breaks down below $[\text{Fe}/\text{H}] \sim -2.5$, and no star has Li abundance comparable to the plateau below $[\text{Fe}/\text{H}] = -4.0$ (e.g., [Ryan et al. 1996, 1999](#); [Bonifacio et al. 2007](#); [Frebel et al. 2008](#); [Aoki et al. 2009](#); [Sbordone et al. 2010](#); [Caffau et al. 2011](#); [Hansen et al. 2014](#); [Bonifacio et al. 2015](#); [Li et al. 2015](#)).

The key stellar metallicity occurs below $[\text{Fe}/\text{H}] \sim -3.0$, especially $\lesssim -3.5$. Stars with $[\text{Fe}/\text{H}] \sim -3.5$ bridge the Spite Plateau stars and ultra metal-poor (UMP; $[\text{Fe}/\text{H}] < -4.0$) stars, all of which exhibit low lithium abundances. However, the current sample size of turn-off stars with $-4.0 < [\text{Fe}/\text{H}] < -3.5$ with available Li measurements is still small, ~ 10 according to the SAGA database ([Suda et al. 2008, 2011](#); [Yamada et al. 2013](#)).

One of the reasons for the small sample size is the rarity of EMP stars. Another is the difficulty of deriving precise abundances for warm EMP stars. In addition to their extremely low metallicity, the relatively high temperatures of main-sequence turn-off stars weaken their absorption lines; higher signal-to-noise ratios for such stars are required for precise abundance measurements.

The purpose of this study is to determine chemical abundances, including Li, for turn-off stars with $[\text{Fe}/\text{H}] < -3.5$. We have obtained high-resolution, high-signal-to-noise ratio spectra with the Subaru Telescope for eight warm EMP stars ($T_{\text{eff}} > 5500$ K, $[\text{Fe}/\text{H}] < -3.0$) previously considered by [Aoki et al. \(2013\)](#); seven of the eight have $[\text{Fe}/\text{H}] < -3.5$. The relatively narrow range of stellar parameters among the sample enable a high-precision differential abundance analysis. Hence, besides understanding the nature of possible Li-depletion mechanisms, these targets are useful for investigation of other elemental abundances for EMP stars. In addition, since our targets have not yet reached the red-giant stage of evolution, we can examine possible abundance changes caused by first dredge-up (e.g., [Spite et al. 2006](#)) from a comparison of the chemical abundances of our targets with those of red giants reported in the literature.

This paper is organized as follows. Details of target selection and observation are described in Section 2. In Section 3, we compare several methods to derive stellar parameters for the eight targets. In addition, we also determine stellar parameters for two bright EMP stars (G 64–12 and LP 815–43) with parallaxes measured by the Gaia satellite. The abundance analysis and its results are described in Section 4. After presenting an interpretation of the results in Section 5, we summarize our conclusions in Section 6.

2. OBSERVATIONS AND REDUCTION

The targets in our present study are selected from [Aoki et al. \(2013\)](#), who reported the results of abundance analysis of snap-shot high-resolution spectroscopy for 137 metal-poor candidates discovered by the Sloan Digital Sky Survey (SDSS; [York et al. 2000](#)) and the Sloan Extension for Galactic Understanding and Exploration (SEGUE; [Yanny et al. 2009](#)). We have obtained new higher-quality spectra for eight targets with the High Dispersion Spectrograph on the Subaru Telescope ([Noguchi et al. 2002](#)). The spectral resolution is $R = 60,000$ with 2×2 CCD binning; the wavelength coverage is $4000 - 6800$ Å. Details of the observations are provided in Table 1. Hereafter, object names are shown using abbreviations, e.g., SDSS J0120–1001 for SDSS J012032.63–100106.5. Although the spectrum of

one of our targets, SDSS J1424+5615, has been analyzed in [Matsumo et al. \(2017\)](#), we re-analyze it in this study.

The data are reduced in a standard manner using the IRAF¹ echelle package, including bias correction, flat fielding, scattered light subtraction, extraction of spectra, and wavelength calibration using Th arc lines. The signal-to-noise ratios per 1.1 km s^{-1} pixel around 6708 \AA and per 1.5 km s^{-1} around 4877 \AA (after re-binning) are estimated from the standard deviation of the continuum level around the Li I doublet at 6708 \AA . Heliocentric radial velocities (v_r) are estimated from Fe lines. Typical uncertainties in v_r are $\sim 1 \text{ km s}^{-1}$. All but one target shows no significant radial velocity changes from [Aoki et al. \(2013\)](#). The exception is SDSS J2349+3832, for which our radial velocity is larger than at the epoch of August 22, 2008 by 3.1 km s^{-1} .

We also analyze the spectra of two bright EMP main-sequence turn-off stars, G 64–12 ($[\text{Fe}/\text{H}] = -3.38$) and LP 815–43 ($[\text{Fe}/\text{H}] = -2.96$). The spectrum of G 64–12 was taken on December 22, 2002 with $R \sim 90,000$ and $S/N \sim 650$ at 6708 \AA ($S/N \sim 454$ at 4880 \AA) ([Aoki et al. 2009](#)). The spectrum of LP 815–43, which was taken from the Subaru archive SMOKA ([Baba et al. 2002](#)), was originally obtained on May 18, 2005 with $R \sim 90,000$ and $S/N \sim 260$ at 6708 \AA ($S/N \sim 142$ at 4880 \AA). Both stars are included in the first data release of the Gaia satellite ([Gaia Collaboration et al. 2016a,b](#)), which allows us to obtain an independent determination of their surface gravities.

3. STELLAR ATMOSPHERIC PARAMETERS

3.1. Methods

In order to establish the most reliable method to derive stellar parameters for EMP turn-off stars, we apply four methods, i) analysis of Balmer-line profiles, ii) spectroscopic analysis of Fe lines, iii) the SEGUE Stellar Parameter Pipeline (SSPP; [Lee et al. 2008a,b](#); [Allende Prieto et al. 2008](#)), and iv) colors (only for T_{eff}), and compare the results. Each method is briefly described below.

3.1.1. Balmer-Line Profiles

Balmer lines of hydrogen are prominent in spectra of warm stars. Their profiles, especially the width of the wings, are sensitive to effective temperature. Contamination arising from metallic absorption lines in the

profiles of Balmer lines is insignificant in EMP stars, with the exception of the $\text{H}\gamma$ line in carbon-enhanced metal-poor (CEMP) stars, which can be impacted by the presence of the CH G -band molecular feature. Our procedure is essentially the same as the method of [Barklem et al. \(2002\)](#), and described in [Matsumo et al. \(2017\)](#). We here briefly summarize our approach, focusing on differences from the previous work.

Careful continuum placement is essential in the analysis of Balmer lines with broad profiles. We estimate the continuum level by interpolating across the blaze functions of adjacent orders containing these lines.

Models of Balmer-line profiles are taken from interpolation of the grid by [Barklem et al. \(2002\)](#)². Atmospheres with $[\text{Fe}/\text{H}] = -3$ and $[\alpha/\text{Fe}] = +0.4$ are assumed throughout the analysis. While the $\text{H}\beta$ line is only sensitive to T_{eff} , $\text{H}\alpha$ is also dependent on surface gravity, $\log g$. Hence, we determine T_{eff} from the $\text{H}\beta$ line first, assuming $\log g = 4.0$, and then determine $\log g$ from the $\text{H}\alpha$ line. We iterate the estimates until the set of $(T_{\text{eff}}, \log g)$ reaches convergence (usually less than three times). Once we obtain the best-fit spectrum from the $\text{H}\beta$ and $\text{H}\alpha$ fitting procedure, we remove possible effects of cosmic rays and absorption lines from the observed spectrum by masking pixels that deviate from the best-fit spectrum by more than 2.5σ . We also modify the fitting region to only include the line wings, defined as the regions where the normalized flux of the best-fit model is between 0.7 and 0.9. We then repeat the fitting until convergence is achieved (usually less than five times).

Errors in our procedure are dominated by uncertainty of the continuum placement. An error of 0.5% in the continuum placement for our sample stars is estimated by applying the interpolating procedure to the orders that contain no broad absorption features. We estimate its effect on T_{eff} and $\log g$ by analyzing the spectra whose continuum level is artificially shifted by 0.5%. In addition, since the estimate of surface gravity is dependent on the assumed T_{eff} , we calculated uncertainties of $\log g$ as follows:

$$\sigma_{\log g}^2 = (\delta \log g)^2 + \left(\frac{\partial \log g}{\partial T_{\text{eff}}}\delta T_{\text{eff}}\right)^2, \quad (1)$$

where δX represents the uncertainties caused by continuum-placement errors, σ_X is the total uncertainties, and X denotes either $\log g$ or T_{eff} . Since $\log g$ does not affect T_{eff} estimates, we adopt $\sigma_{T_{\text{eff}}} = \delta T_{\text{eff}}$. The

¹ IRAF is distributed by the National Optical Astronomy Observatory, which is operated by the Association of Universities for Research in Astronomy, Inc. under cooperative agreement with the National Science Foundation.

² <http://www.astro.uu.se/%7ebarklem/>

Table 1. Observation Log for the SDSS Sample

Object Name ^a	Observing run (yyyy-mm-dd)	V (mag)	Exp. time (s)	S/N @4877 Å	S/N @6708 Å	v_r (km s ⁻¹)
SDSS J012032.63–100106.5	2009-09-10,12	16.55	14490	34	66	-58.6
SDSS J103649.93+121219.8	2009-11-24	15.50	6514	37	50	-33.8
SDSS J142441.88+561535.0	2009-06-28,29,07-01	15.70	13800	76	85	0.0
SDSS J152202.09+305526.3	2009-06-28,29	16.42	21600	60	69	-354.8
SDSS J164005.30+370907.8	2009-06-28,29	15.55	14400	95	95	-51.6
SDSS J200513.48–104503.2	2009-09-12	16.78	12000	31	40	-55.8
SDSS J230959.55+230803.0	2009-11-24	17.02	12000	20	36	-307.0
SDSS J234939.71+383217.8	2009-09-10,12	16.80	19200	38	60	-84.2

NOTE—Objects IDs given by SDSS can be found in [Aoki et al. \(2013\)](#).

^aThe object name is an abbreviation, and is used throughout the rest of this paper, e.g., SDSS J0120–1001 for SDSS J012032.63–100106.5.

covariance can be found in a similar manner:

$$\sigma_{T_{\text{eff}} \log g} = \frac{\partial \log g}{\partial T_{\text{eff}}} \sigma_{T_{\text{eff}}}^2. \quad (2)$$

Since covariances contribute to the total errors of our derived abundances, they need to be taken into account.

We finally check the fitting results by eye. The fitting results for SDSS J1424+5615 are shown in Figure 1.

Although the microturbulent velocity (v_t) is not required for the Balmer-line analysis, it needs to be determined for the abundance analysis. The microturbulent velocity is not derived from the Balmer-line profiles, but is determined so that abundances derived from individual neutral Fe lines exhibit no trends with the strengths of the lines. The uncertainty of v_t , expressed as δv_t , is determined so that the trend is not significant at greater than the 1σ level. In addition, we also examine the uncertainties of v_t due to the errors in T_{eff} and $\log g$.

3.1.2. Fe-Lines Method

This method determines stellar parameters from an analysis of Fe absorption lines in a spectrum, those that result in no dependence on the ionization stage, excitation potential, or strength of the individual lines.

Suppose that EW_i is the equivalent width of an Fe line and A_i is the Fe abundance determined from the line. In order to determine stellar parameters, we evaluate three probabilities:

- 1 p_{ex} : Probability that the correlation between completely uncorrelated sets of values becomes larger than the observed correlation between A_i and excitation energy.

- 2 p_{ion} : Probability that a difference between Fe abundances determined from neutral species and ionized species becomes larger than the observed difference due only to measurement errors.

- 3 p_{ew} : Probability that a correlation between completely uncorrelated set of values becomes larger than the observed correlation between A_i and the normalized equivalent width, $\log(EW_i/\lambda)$.

The probabilities p_{ex} and p_{ew} are evaluated using Spearman’s rank correlation test. This is because the expected correlations are not necessarily linear, especially for the correlation between $\log(EW_i/\lambda_i)$ and A_i . Then, we search for the combination of stellar parameters (T_{eff} , $\log g$, v_{turb}) which maximizes $p = p_{\text{ex}} \cdot p_{\text{ion}} \cdot p_{\text{ew}}$. The [Fe/H] of the model atmosphere is also forced to agree with the derived [Fe/H] within 0.3 dex.

Uncertainties are estimated using a confidence-region boundary, where $p = 0.317p_{\text{max}}$, assuming it to be a 3-D ellipsoid. Covariances of any pair of the two parameters are also estimated.

Determination of stellar parameters from Fe lines fully relies on model atmospheres, and could be significantly affected by deviation from local thermodynamic equilibrium (non-LTE, NLTE) and the effect of 3D motions in the atmosphere. The NLTE/3D effects might be significantly large for EMP stars ([Asplund 2005](#)). In a limited range of T_{eff} and [Fe/H], however, the correction should be systematic. For example, the difference between the Fe abundance derived from an NLTE analysis of the Fe I lines and that from an LTE analysis varies less

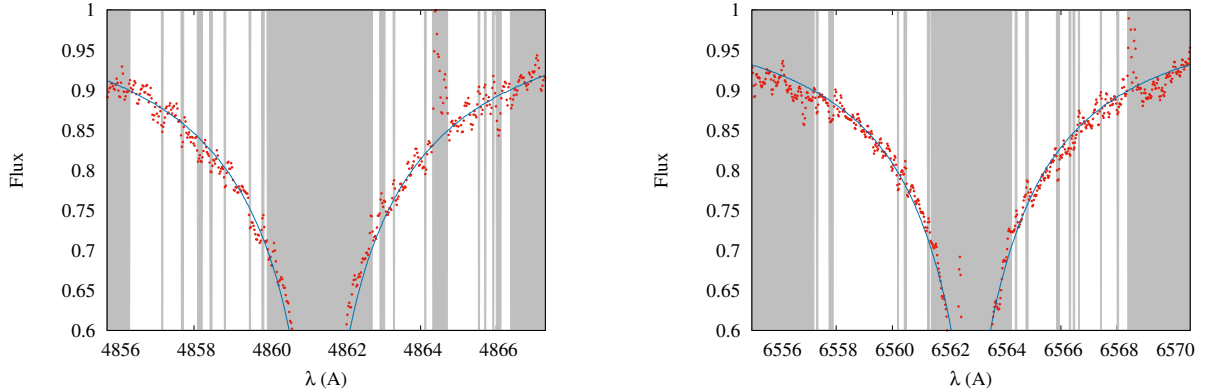


Figure 1. Fitting results for the $H\beta$ line (left panel) and $H\alpha$ line (right panel) of SDSS J1424+5615. Red points show the observed normalized spectrum and the blue line shows the best-fit model spectrum. To avoid the effects of cosmic rays and/or absorption lines, and to perform the fitting of the line wings, the grey shaded regions are excluded from the fitting procedure (see text for details).

than 0.1 dex within the parameter range of our targets (Lind et al. 2012). In order to avoid such systematic effects, we carry out a line-by-line differential analysis adopting a well-studied bright EMP turn-off star, G 64–12, as a reference star. For each line, we first determine the difference in abundance (ΔA_i) between the target and G 64–12, and then convert it to the abundance of the star A_i by

$$A_i = \langle A[\text{G 64–12}] \rangle + \Delta A_i. \quad (3)$$

3.1.3. SSPP-, Color-, & Parallax-Based Stellar Parameter Estimates

Effective temperatures estimated by the SSPP, and given in Data Release 7 (DR7) of the SDSS, were adopted by Aoki et al. (2013) for their sample of stars, from which our targets are selected. However, as the SSPP has continued to be updated, here we adopt T_{eff} and $\log g$ estimates derived by the latest version. The update results in higher T_{eff} by ~ 100 K.

We also derive effective temperatures from photometric colors, for a comparison of stellar parameters estimated by different methods. We first convert g -, r -, and i -band **psfMag** measured in the SDSS survey to the Johnson-Cousin B , V , R_c , and I_c system using the formulae provided by Jordi et al. (2006) for Population II stars. Since SDSS photometry of G 64–12 and LP 815–43 suffer from saturation, we adopt the APASS V magnitudes for these two targets (Henden et al. 2016). Infrared photometric data are taken from Two-Micron All-Sky Survey (2MASS; Cutri et al. 2003). After correcting for extinction from Schlafly & Finkbeiner (2011), we derive effective temperatures from $V - K_s$ colors using the calibration of Casagrande et al. (2010), with the assumption of $[\text{Fe}/\text{H}] = -3.5$. These two methods are based on calibrations using bright and/or

nearly standard stars to establish the scale. Since EMP turn-off stars are rare, the uncertainties could be larger than those for less metal-poor stars.

The stars G 64–12 and LP 815–43 are both included in the Data Release 1 of Gaia. We calculated their luminosities using the Gaia parallaxes, the bolometric correction of Casagrande et al. (2010), and V and K_s band magnitudes. Surface gravity is then derived from the following equation:

$$\log g = \log g_{\odot} + \log(M/M_{\odot}) + 4 \log(T_{\text{eff}}/T_{\text{eff},\odot}) - \log(L/L_{\odot}), \quad (4)$$

where M is the mass of the stars, assumed to be $0.75 M_{\odot}$, and L is the luminosity of the stars. We adopt $\log g_{\odot} = 4.438$ and $T_{\text{eff}} = 5777$ K as the solar values.

3.2. Results

3.2.1. Results for Bright EMP Stars

Before discussing our SDSS program stars, we present results for G 64–12 and LP 815–43, as a check on both the absolute and relative scales of the derived stellar parameters in this work. Note that LP 815–43 is analysed only for the evaluation of the relative scale, and is not included in the subsequent abundance analysis.

Stellar parameter estimates for G 64–12 and LP 815–43 are summarized in Table 2. They are also shown in Figure 2 and Figure 3. We note that the result for the Balmer-line analysis of G 64–12 is slightly different from our previous work (Matsuno et al. 2017), due to small changes in the algorithm. The difference is still within the quoted uncertainty.

Results from the Balmer-line profile analysis agree with those obtained from the Fe lines analysis within the errors. On the other hand, there appears to be a systematic difference between the Balmer-line T_{eff} estimates and the color-based T_{eff} estimates, by 100–150 K

(Aoki et al. 2006; Norris et al. 2013a). A high-precision analysis of G 64–12 has been carried out in previous studies (Placco et al. 2016; Reggiani et al. 2016), and obtained $T_{\text{eff}} = 6463$ K (Meléndez et al. 2010) and $\log g = 4.26$ (Nissen et al. 2007). While our temperature estimate based on the Balmer-line analysis is lower than theirs, our color-based temperature estimate is consistent. See Matsuno et al. (2017) for the detailed comparison among derived effective temperatures of G 64–12 in previous studies.

Since a differential analysis is conducted in this work, the differences in the estimated parameters between a target star and the reference star (G 64–12) are important. The symbol “ Δ ” listed in Table 2 describes this difference for parameters derived for G 64–12 and LP 815–43. The effective temperature of LP 815–43 determined by each method is slightly higher than that of G 64–12, whereas the $\log g$ of LP 815–43 is slightly lower than that of G 64–12. We conclude that relative differences of parameters are not so affected by the choice of the methods, even though a small offset exists between individual methods.

3.2.2. Results for the SDSS Sample

Results for our program sample of SDSS stars are summarized in Table 3 and shown in Figure 2. Two out of the eight stars contain only a small number of Fe absorption lines, and thus are not suitable for spectroscopic determination of stellar parameters from Fe lines. For two other stars, the set of stellar parameters which simultaneously satisfy the three requirements listed in Section 3.1.2 above are not found. The results based on the Fe-lines analysis for these four stars are excluded from Table 3.

A comparison of the results obtained by the different methods we consider is presented in Figure 2 and Figure 3. As can be seen, in most cases, the parameters from the Fe-lines analysis are in agreement with those from the Balmer-line profiles within the uncertainties, though the errors are large. We note that no offset is expected due to the differential analysis. On the other hand, there is a systematic difference in T_{eff} between the SSPP-based estimates and the Balmer-line analysis, which could be related to the known difference between T_{eff} from Balmer-line analysis and photometric T_{eff} estimates (Norris et al. 2013a). We note that Aoki et al. (2013) adopted T_{eff} estimated by a previous version of SSPP, which are systematically lower than the present one. Hence, the difference between our results of the Balmer line analysis and those of Aoki et al. (2013) is about 100 K smaller.

Table 2. Comparison of Stellar Parameters for G 64–12 and LP 815–43

Method	Parameter	G 64–12	LP 815–43	Δ^a
Balmer lines	T_{eff} (K)	6285	6323	38
	$\sigma_{T_{\text{eff}}}$ (K)	26	31	40
	$\log g$	4.30	4.21	-0.09
	$\sigma_{\log g}$	0.15	0.17	0.23
	v_t (km s $^{-1}$)	1.32	1.62	0.30
Fe lines ^b	σ_{v_t} (km s $^{-1}$)	0.18	0.19	0.26
	T_{eff} (K)	(6285)	6424	139
	$\sigma_{T_{\text{eff}}}$ (K)	...	83	79
	$\log g$	(4.30)	4.22	-0.08
	$\sigma_{\log g}$...	0.20	0.13
Color ($V - K_s$)	v_t (km s $^{-1}$)	(1.32)	1.54	0.22
	σ_{v_t} (km s $^{-1}$)	...	0.17	0.09
	T_{eff} (K)	6434	6481	47
Parallax	$\sigma_{T_{\text{eff}}}$ (K)	55	67	87
	$\log g$	4.23	4.15	-0.08
	$\sigma_{\log g}$	0.16	0.13	0.21

^aErrors in Δ for the stellar parameters are quadratic sums of the errors for the individual stars, except for the Fe-lines method, for which errors of LP 815–43 are the quadratic sums of the errors of G 64–12 and the error in Δ .

^bSpectroscopic parameters are determined using G 64–12 as a reference star, using the listed parameters for this star.

Contrary to what was found from the analysis of G 64–12 and LP 815–43, we do not find any systematic difference in effective temperature estimates between the Balmer-line analysis and $V - K_s$ color approach. Although Aoki et al. (2013) reached the conclusion that the offset in T_{eff} between $V - K_s$ color and the SSPP is small for their sample with $[\text{Fe}/\text{H}] < -2.5$, the latest version of the SSPP appears to over-estimate T_{eff} compared to the $V - K_s$ color technique for EMP turn-off stars. There is also a difference between the dust map adopted to correct for interstellar extinction between the present analysis and that used by Aoki et al. (2013). We note that the comparison here only includes a small sample in the present study, and that the T_{eff} derived from colors could be affected by large errors in the K_s band magnitude of 2MASS for these fainter stars.

Uncertainties in the Balmer-line analysis are dominated by the continuum placement, which does not significantly depend on S/N for our sample stars. There-

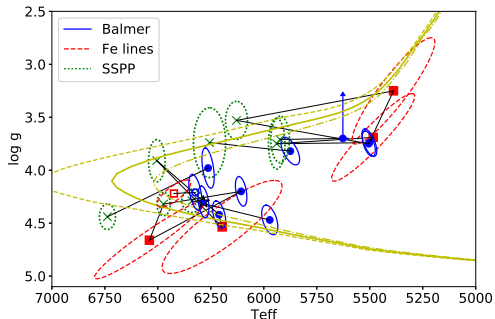


Figure 2. Stellar parameters for our program stars in an H-R diagram, together with α -enhanced Y^2 isochrones with $[\text{Fe}/\text{H}] = -3.0$ and ages of 10, 12, and 14 Gyr, which are shown as dot-dashed, solid, and dashed yellow lines, respectively (Kim et al. 2002). The results of the analysis of Balmer-line profiles are shown with blue filled circles, those of the Fe-lines analysis are shown with red squares, and those of the SSPP are shown with green crosses. The results for the same star are connected with black lines, and 1σ uncertainties are shown with ellipses. The result of the Balmer-line analysis for G 64–12 is shown with a blue star. LP 815–43 is shown with open symbols. The SDSS program stars are shown with filled symbols.

fore, we adopt the results derived from the analysis of Balmer-line profiles in the abundance analysis described below. The Balmer-line analysis failed to determine the $\log g$ for SDSS J0120–1001, due to the limited range of the grid (for $T_{\text{eff}} \geq 5600$ K, only $\log g \geq 3.4$ is covered). In addition, the $\log g$ sensitivity of $\text{H}\alpha$ lines dramatically decreases at $\log g \lesssim 3.4$. Considering the similarity of the SSPP $\log g$ between SDSS J1036+1212, SDSS J1522+3055, and SDSS J0120–1001, we adopt $\log g = 3.4 \pm 0.3$ for the abundance analysis of this star.

Behara et al. (2010) also analyzed our program star SDSS J1036+1212. Their T_{eff} estimate is based on the $\text{H}\alpha$ wing, and the $\log g$ estimate is based on ionization balance between Fe I and Fe II. They obtained $T_{\text{eff}} = 6000$ K and $\log g = 4.0$, which are ~ 500 K and 0.3 dex higher than our results. The T_{eff} derived from the $V-K_s$ color is somewhat closer, but still 300 K cooler than their result. The source of the difference is not clear, because their methods and ours are similar. There is another discrepancy between the present study and Behara et al. (2010). It concerns the Eu abundance, and is discussed in Section 5.4.

The adopted microturbulent velocities are listed in Table 4. For SDSS J2309+2308 and SDSS J2005–1045, v_t is not well-constrained due to the small number of Fe absorption lines in these spectra. We adopt $v_t = 1.0 \pm 0.5 \text{ km s}^{-1}$ for these targets.

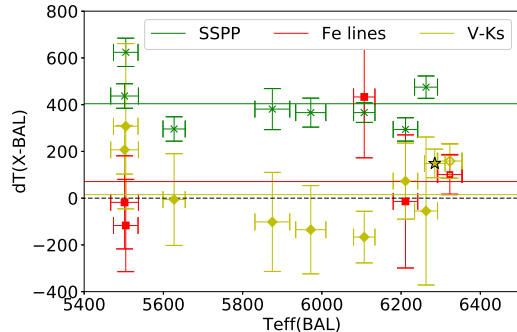


Figure 3. Differences of the effective temperatures estimated by the analysis of Balmer-line profiles from those obtained by other methods. The symbols are the same as in Figure 2, except yellow diamonds indicate the results of the $V - K_s$ color-based estimate using the approach of Casagrande et al. (2010). Horizontal solid lines show the unweighted mean of the differences for each method for the SDSS program stars (for SSPP, $\langle \Delta T \rangle = 404$ K; for the Fe-lines analysis, $\langle \Delta T \rangle = 71$ K; for $V - K_s$ color, $\langle \Delta T \rangle = 15$ K). The black dashed line shows $\Delta T = 0$.

4. CHEMICAL ABUNDANCES

4.1. Abundance Analysis

We use 1D LTE model atmospheres from the ATLAS NEWODF grid with $[\alpha/\text{Fe}] = +0.4$ (Castelli & Kurucz 2003) in the abundance analysis. Abundances are determined differentially with respect to the reference star G 64–12, as described in Section 3.1.2.

The line list used in the present work is based on that of Aoki et al. (2013), updated to include recently published gf -values. We then restrict the list to the lines identified in the spectrum of G 64–12. Because of a slight difference in instrument setting, our spectrum of G 64–12 does not cover wavelengths shorter than 4100 Å. In order to efficiently utilize the spectra of the SDSS sample, we also include Mn I 4044 Å, Fe I 4046 Å, Fe I 4064 Å, and Sr II 4078 Å, whose equivalent widths of G 64–12 are taken from Reggiani et al. (2016).

The equivalent width of each absorption line is measured by Gaussian fitting, and listed in Table 5. The continuum level is estimated by comparing the spectrum of the targets with that of G 64–12. The widths of the absorption lines are dominated by instrumental broadening and macroturbulence, and exclude the possibility of rapid rotation for our sample stars.

In addition, we include the line list for the CH G -band from Masseron et al. (2014) and the line list of ^7Li from Smith et al. (1998). We determine abundances from spectrum synthesis using 4222.8 – 4325.4 Å for the CH G -band and 6707.4 – 6708.2 Å for the Li I doublet.

Table 3. Stellar Parameters for the SDSS Sample

Object	Balmer				Fe lines ^a				SSPP				$V - K_s$	
	T_{eff} (K)	σ (K)	$\log g$ (dex)	σ (dex)	T_{eff} (K)	σ (K)	$\log g$ (dex)	σ (dex)	T_{eff} (K)	σ (K)	$\log g$ (dex)	σ (dex)	T_{eff} (K)	σ (K)
SDSS J0120-1001	5627	28	< 3.70 ^b	5923	44	3.71	0.22	5621	194
SDSS J1036+1212	5502	35	3.74	0.13	5484	196	3.69	0.41	5939	39	3.75	0.24	5709	98
SDSS J1424+5615	6107	27	4.20	0.14	6540	259	4.66	0.37	6473	32	4.32	0.11	5940	107
SDSS J1522+3055	5505	31	3.75	0.12	5388	195	3.25	0.50	6129	52	3.53	0.18	5813	352
SDSS J1640+3709	6211	31	4.42	0.13	6197	283	4.54	0.44	6505	39	3.91	0.20	6284	160
SDSS J2005-1045	6263	29	3.98	0.19	6738	38	4.44	0.12	6208	315
SDSS J2309+2308	5875	44	3.82	0.13	6256	76	3.74	0.33	5773	207
SDSS J2349+3832	5972	38	4.47	0.14	6338	49	4.29	0.11	5837	185

^aWe use the stellar parameters of G 64-12 derived from Balmer line profiles as a reference.

^b3.40 is adopted in the abundance analysis.

Table 4. Microturbulent Velocities and Metallicities of Program Stars

Object	v_t km s^{-1}	σ_{v_t} km s^{-1}	[Fe/H]	$\sigma_{[\text{Fe}/\text{H}]}$
G 64-12	1.32	0.18	-3.38	0.02
SDSS J0120-1001	0.99	0.48	-3.84	0.06
SDSS J1036+1212	0.54	0.36	-3.62	0.06
SDSS J1424+5615	0.97	0.24	-3.10	0.03
SDSS J1522+3055	0.33	0.32	-3.94	0.05
SDSS J1640+3709	1.19	0.38	-3.54	0.05
SDSS J2005-1045	1.00	0.53	-3.86	0.13
SDSS J2309+2308	1.00	0.50	-3.96	0.09
SDSS J2349+3832	0.80	0.54	-3.73	0.07

Table 5. Measured Equivalent Widths

Object	Species	Wavelength (Å)	ExPot (eV)	log(gf)	EW (mÅ)	Reference
G 64–12	Na I	5889.951	0.000	0.101	32.8	1
G 64–12	Na I	5895.924	0.000	-0.197	19.0	1
G 64–12	Mg I	4167.271	4.346	-0.710	4.0	2
G 64–12	Mg I	4702.991	4.330	-0.380	9.4	2
G 64–12	Mg I	5172.684	2.712	-0.450	77.4	3

NOTE— 1: Morton (1991), 2: Froese Fischer (1975), 3: Aldenius et al. (2007), 4: Wiese & Martin (1980), 5: Smith & Raggett (1981), 6: Ivans et al. (2006), 7: Lawler & Dakin (1989), 8: Piskunov et al. (1995), 9: Lawler et al. (2013), 10: Grevesse et al. (1989), 11: Wood et al. (2013), 12: Pickering et al. (2001), 13: Ryabchikova et al. (1994), 14: Martin et al. (1988), 15: Sobeck et al. (2007), 16: O’Brian et al. (1991), 17: Fuhr et al. (1988), 18: Bard et al. (1991), 19: Meléndez & Barbuy (2009), 20: Moity (1983), 21: Pinnington et al. (1995), 22: Grevesse et al. (1981), 23: Grevesse et al. (2015)

NOTE—Table 5 is published in its entirety in the machine-readable version. A portion is shown here for guidance regarding its form and content.

We adopt the mean of the abundances determined from individual lines for each species. Uncertainties are determined as follows:

$$\sigma(X) = \sqrt{\sigma_{\text{lines}}^2/N + \sigma_{\text{atm}}^2}, \quad (5)$$

where σ_{lines} is the standard deviation of abundances determined from individual lines, and N is the number of lines used in the analysis. When $N < 3$, we take σ_{FeI} as σ_{lines} . The variable σ_{atm} is the uncertainty due to uncertainties in the stellar parameter estimates expressed as:

$$\sigma_{\text{atm}}^2 = \sum_{i=1}^4 \left(\frac{\partial \log \epsilon}{\partial X_i} \sigma_{X_i} \right)^2 + \sum_{i \neq j} \frac{\partial \log \epsilon}{\partial X_i} \frac{\partial \log \epsilon}{\partial X_j} \sigma_{X_i X_j}, \quad (6)$$

where $(X_1, X_2, X_3, X_4) = (T_{\text{eff}}, \log g, v_t, [\text{Fe}/\text{H}])$.

In cases where no absorption lines are detected for a specific element, we place conservative 5σ upper limits on the equivalent widths, as the upper limits on equivalent widths do not contradict with the equivalent widths of lines that are detected in the spectrum. These 5σ upper limits are also placed on Li and C abundances from spectral synthesis.

Note that our analysis is carried out differentially on the scale of G 64–12. Therefore, when one compares the abundances with other papers, it is required to include the uncertainty in abundances of G 64–12. In particular, NLTE could significantly affect some elements, and 3D effects may play a major role on the strengths of the molecular lines.

4.2. Results

Results of the abundance analysis are listed in Table 6 (metallicities are listed in Table 4). The results are also displayed in Figure 4. Note that the metallicities for all but one of our program stars (7 of 8) are $[\text{Fe}/\text{H}] < -3.5$.

The stars G 64–12 and SDSS J1424+5615 have been previously analyzed in Matsuno et al. (2017). As the line list and some algorithms employed have been updated, the derived abundances for these stars are not exactly the same. The difference is $\lesssim 0.05$ dex for G 64–12, and $\lesssim 0.2$ dex for SDSS J1424+5615 (~ 0.4 dex for $[\text{C}/\text{Fe}]$). The larger difference for SDSS J1424+5615 is because we derive abundances differentially in this study. Note that we are able to derive a C abundance estimate for G 64–12, which was not derived in Matsuno et al. (2017). Although the redder part of the fitting region in our spectrum is significantly affected by bad columns in the CCD, the bluer part turns out to have sufficiently high quality to derive a C abundance ($\lesssim 4324.5$ Å). The carbon ($[\text{C}/\text{Fe}] = +0.92$) and barium ($[\text{Ba}/\text{Fe}] = -0.07$) abundance ratios of G 64–12 are consistent with its classification as a CEMP star with no enhancement of neutron-capture elements (CEMP-no; Beers & Christlieb 2005), if we adopt $[\text{C}/\text{Fe}] > +0.7$ as the CEMP criterion (Placco et al. 2016).

Whereas $\log g$ estimates in most previous studies are determined from ionization balance of Fe I and Fe II lines, here we adopt $\log g$ estimated from Balmer-line profiles. We detect Fe II lines for seven objects, for

all of which the difference in Fe abundances from Fe II lines and from Fe I lines is consistent with the difference of G 64–12 (0.11 dex) within 2σ , and for five of which the differences are within 1σ (Figure 4). This result indicates that the abundance results of the present work does not essentially change even if the $\log g$ is estimated from a Fe I/II balance.

4.2.1. Carbon

Two stars in our SDSS program sample exhibit significant carbon enhancement ($[C/Fe] > +1.0$). One is SDSS J1036+1212 ($[C/Fe] = +1.19$) with a high Ba abundance ($[Ba/Fe] = +1.68$). The metallicity of this star is $[Fe/H] = -3.62$, which makes this star one of the most metal-poor CEMP-*s* stars (CEMP stars with *s*-process enhancements; Beers & Christlieb 2005). The Sr abundance of this star is low, which is a characteristic feature of CEMP-*s* stars. Although the abundances of SDSS J1036+1212 derived in this work and those derived by Behara et al. (2010) differ, due to different choice of effective temperature, high C, Ba and low Sr abundances are obtained by both studies. The other CEMP star is SDSS J1424+5615, which has been studied in Matsuno et al. (2017). Interestingly, both of the stars show large Na enhancements (Table 6).

There is another star, SDSS J2309+2308, which exhibits Na and Ba excesses, although its Ba abundance relies on only one Ba II line at 4554 Å. This object

could also be a CEMP-*s* star. The upper limit on C ($[C/Fe] < +2.0$) is insufficient to determine whether this star is C-rich or not. The reported upper limits on C abundance for most of our SDSS program stars are not sufficiently low to identify them as C-normal stars.

Although Eu abundances for the C-rich stars is important to identify “CEMP-*i*” stars (Hampel et al. 2016), the relatively high temperatures of our SDSS program stars prevents determination of meaningful limits for their Eu abundances based on our present data.

4.2.2. Lithium

The Li abundance we obtain for G 64–12 places it on the Spite Plateau, similar to those reported by previous studies, confirming that our analysis is consistent in the framework of 1D/LTE analysis. SDSS J1424+5615, which has the highest metallicity among stars in our sample ($[Fe/H] = -3.10$), has a comparable Li abundance as G 64–12. By contrast, all stars with $[Fe/H] < -3.5$ in our sample have lithium abundances less than $A(Li) = 2.0$. This extends the previously found decreasing trend of lithium toward the lowest metallicity to $[Fe/H] \sim -4$ (Bonifacio et al. 2007; Aoki et al. 2009; Sbordone et al. 2010). The Li abundances are compared with previous studies and discussed in detail in Section 5.

Table 6. Results of the Chemical Abundance Analysis

Object	Species	N	$\log \epsilon(X)$	σ	$[X/Fe]^a$	σ
G 64–12	Li I	1	2.22	0.07	5.60	0.07
G 64–12	C (CH)	1	5.97	0.07	0.92	0.07
G 64–12	Na I	2	2.80	0.06	-0.07	0.05
G 64–12	Mg I	5	4.60	0.05	0.37	0.04
G 64–12	Ca I	15	3.44	0.02	0.48	0.02
G 64–12	Ti I	6	2.25	0.04	0.67	0.03
G 64–12	Cr I	6	2.11	0.03	-0.15	0.02
G 64–12	Fe I	78	4.12	0.02	0.00	0.01
G 64–12	Sc II	5	-0.02	0.07	0.21	0.08
G 64–12	Ti II	17	2.11	0.06	0.53	0.06
G 64–12	Fe II	15	4.23	0.06	0.11	0.07
G 64–12	Sr II	2	-0.33	0.08	0.18	0.08
G 64–12	Ba II	2	-1.27	0.07	-0.07	0.07

Table 6 continued

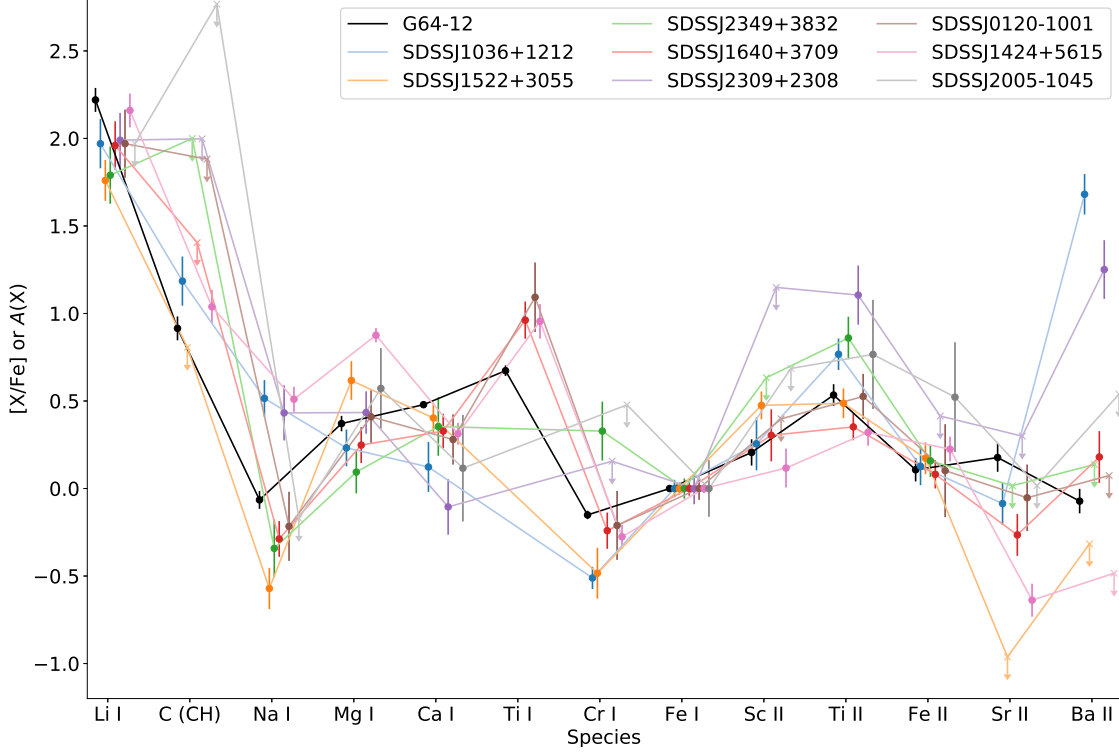


Figure 4. Chemical abundances of our program stars. Abundances are determined differentially using G 64–12 as a reference (abundances are shown with black dots and a solid line). The Li abundances are provided as $A(\text{Li})$, while the abundances of other elements are provided as $[\text{X}/\text{Fe}]$. Data points are slightly horizontally shifted for clarity.

Table 6 (*continued*)

Object	Species	N	$\log \epsilon(\text{X})$	σ	$[\text{X}/\text{Fe}]^a$	σ
SDSS J0120–1001	Li I	1	1.97	0.19	5.81	0.19
SDSS J0120–1001	C (CH)	...	< 6.47	...	< 1.88	...
SDSS J0120–1001	Na I	1	2.18	0.19	-0.22	0.20
SDSS J0120–1001	Mg I	2	4.17	0.15	0.41	0.15
SDSS J0120–1001	Ca I	2	2.78	0.14	0.28	0.14
SDSS J0120–1001	Ti I	1	2.20	0.19	1.09	0.20
SDSS J0120–1001	Cr I	1	1.59	0.19	-0.21	0.20
SDSS J0120–1001	Fe I	17	3.66	0.07	0.00	0.06
SDSS J0120–1001	Sc II	...	< -0.29	...	< 0.40	...
SDSS J0120–1001	Ti II	4	1.63	0.12	0.53	0.13
SDSS J0120–1001	Fe II	3	3.76	0.26	0.10	0.27
SDSS J0120–1001	Sr II	2	-1.02	0.20	-0.05	0.19
SDSS J0120–1001	Ba II	...	< -1.59	...	< 0.07	...
SDSS J1036+1212	Li I	1	1.97	0.14	5.59	0.14
SDSS J1036+1212	C (CH)	1	6.00	0.14	1.19	0.14

Table 6 continued

Table 6 (continued)

Object	Species	N	$\log \epsilon(X)$	σ	$[X/Fe]^a$	σ		
SDSS J1036+1212	Na I	2	3.14	0.10	0.51	0.10		
SDSS J1036+1212	Mg I	2	4.22	0.11	0.23	0.10		
SDSS J1036+1212	Ca I	1	2.85	0.14	0.12	0.14		
SDSS J1036+1212	Cr I	3	1.51	0.06	-0.51	0.06		
SDSS J1036+1212	Fe I	15	3.88	0.06	0.00	0.05		
SDSS J1036+1212	Sc II	1	-0.21	0.14	0.25	0.15		
SDSS J1036+1212	Ti II	10	2.10	0.07	0.77	0.09		
SDSS J1036+1212	Fe II	3	4.01	0.09	0.13	0.11		
SDSS J1036+1212	Sr II	2	-0.83	0.12	-0.09	0.12		
SDSS J1036+1212	Ba II	2	0.25	0.12	1.68	0.12		
SDSS J1424+5615	Li I	1	2.16	0.10	5.26	0.10		
SDSS J1424+5615	C (CH)	1	6.37	0.10	1.04	0.10		
SDSS J1424+5615	Na I	2	3.65	0.07	0.51	0.07		
SDSS J1424+5615	Mg I	5	5.38	0.05	0.88	0.04		
SDSS J1424+5615	Ca I	5	3.56	0.06	0.31	0.06		
SDSS J1424+5615	Ti I	1	2.81	0.10	0.96	0.10		
SDSS J1424+5615	Cr I	3	2.27	0.07	-0.28	0.07		
SDSS J1424+5615	Fe I	25	4.40	0.03	0.00	0.03		
SDSS J1424+5615	Sc II	1	0.17	0.11	0.12	0.11		
SDSS J1424+5615	Ti II	6	2.17	0.07	0.32	0.08		
SDSS J1424+5615	Fe II	4	4.63	0.06	0.23	0.07		
SDSS J1424+5615	Sr II	2	-0.87	0.09	-0.64	0.09		
SDSS J1424+5615	Ba II	...	<	-1.40	...	<	-0.48	...
SDSS J1522+3055	Li I	1	1.76	0.11	5.70	0.11		
SDSS J1522+3055	C (CH)	...	<	5.30	...	<	0.81	...
SDSS J1522+3055	Na I	1	1.73	0.12	-0.57	0.12		
SDSS J1522+3055	Mg I	4	4.28	0.12	0.62	0.11		
SDSS J1522+3055	Ca I	2	2.81	0.08	0.40	0.09		
SDSS J1522+3055	Cr I	3	1.22	0.14	-0.48	0.15		
SDSS J1522+3055	Fe I	21	3.56	0.05	0.00	0.04		
SDSS J1522+3055	Sc II	3	-0.31	0.07	0.48	0.08		
SDSS J1522+3055	Ti II	9	1.50	0.07	0.49	0.08		
SDSS J1522+3055	Fe II	3	3.74	0.08	0.17	0.09		
SDSS J1522+3055	Sr II	...	<	-2.03	...	<	-0.96	...
SDSS J1522+3055	Ba II	...	<	-2.07	...	<	-0.32	...
SDSS J1640+3709	Li I	1	1.96	0.14	5.50	0.14		
SDSS J1640+3709	C (CH)	...	<	6.30	...	<	1.41	...

Table 6 continued

Table 6 (continued)

Object	Species	N	$\log \epsilon(X)$	σ	$[X/Fe]^a$	σ		
SDSS J1640+3709	Na I	2	2.42	0.10	-0.29	0.10		
SDSS J1640+3709	Mg I	2	4.31	0.11	0.25	0.10		
SDSS J1640+3709	Ca I	4	3.13	0.09	0.33	0.10		
SDSS J1640+3709	Ti I	2	2.38	0.10	0.96	0.11		
SDSS J1640+3709	Cr I	2	1.86	0.10	-0.24	0.10		
SDSS J1640+3709	Fe I	22	3.96	0.05	0.00	0.04		
SDSS J1640+3709	Sc II	1	-0.08	0.14	0.30	0.15		
SDSS J1640+3709	Ti II	6	1.77	0.06	0.35	0.08		
SDSS J1640+3709	Fe II	3	4.05	0.06	0.08	0.08		
SDSS J1640+3709	Sr II	2	-0.93	0.13	-0.26	0.12		
SDSS J1640+3709	Ba II	1	-1.17	0.15	0.18	0.15		
SDSS J2005-1045	Li I	...	<	1.97	...	<	5.83	...
SDSS J2005-1045	C (CH)	...	<	7.34	...	<	2.77	...
SDSS J2005-1045	Na I	...	<	2.21	...	<	-0.17	...
SDSS J2005-1045	Mg I	3		4.31	0.21		0.57	0.23
SDSS J2005-1045	Ca I	1		2.60	0.28		0.12	0.30
SDSS J2005-1045	Cr I	...	<	2.26	...	<	0.48	...
SDSS J2005-1045	Fe I	6		3.64	0.13		0.00	0.16
SDSS J2005-1045	Sc II	...	<	-0.02	...	<	0.69	...
SDSS J2005-1045	Ti II	1		1.86	0.29		0.77	0.31
SDSS J2005-1045	Fe II	1		4.17	0.29		0.52	0.31
SDSS J2005-1045	Sr II	...	<	-0.97	...	<	0.02	...
SDSS J2005-1045	Ba II	...	<	-1.14	...	<	0.54	...
SDSS J2309+2308	Li I	1		1.99	0.14		5.95	0.14
SDSS J2309+2308	C (CH)	...	<	6.47	...	<	2.00	...
SDSS J2309+2308	Na I	1		2.71	0.15		0.43	0.16
SDSS J2309+2308	Mg I	2		4.08	0.13		0.43	0.12
SDSS J2309+2308	Ca I	1		2.28	0.15		-0.10	0.16
SDSS J2309+2308	Cr I	...	<	1.84	...	<	0.16	...
SDSS J2309+2308	Fe I	5		3.54	0.09		0.00	0.09
SDSS J2309+2308	Sc II	...	<	0.34	...	<	1.15	...
SDSS J2309+2308	Ti II	1		2.10	0.15		1.10	0.17
SDSS J2309+2308	Fe II	...	<	3.96	...	<	0.41	...
SDSS J2309+2308	Sr II	...	<	-0.79	...	<	0.30	...
SDSS J2309+2308	Ba II	1		-0.53	0.17		1.25	0.17
SDSS J2349+3832	Li I	1		1.79	0.16		5.52	0.16
SDSS J2349+3832	C (CH)	...	<	6.70	...	<	2.00	...

Table 6 continued

Table 6 (continued)

Object	Species	N	$\log \epsilon(X)$	σ	$[X/Fe]^a$	σ
SDSS J2349+3832	Na I	1	2.17	0.17	-0.34	0.17
SDSS J2349+3832	Mg I	2	3.96	0.14	0.09	0.12
SDSS J2349+3832	Ca I	1	2.96	0.16	0.35	0.17
SDSS J2349+3832	Cr I	1	2.24	0.16	0.33	0.17
SDSS J2349+3832	Fe I	15	3.77	0.08	0.00	0.06
SDSS J2349+3832	Sc II	... <	0.05	... <	0.63	...
SDSS J2349+3832	Ti II	3	2.08	0.11	0.86	0.12
SDSS J2349+3832	Fe II	3	3.93	0.06	0.16	0.09
SDSS J2349+3832	Sr II	... <	-0.84	... <	0.02	...
SDSS J2349+3832	Ba II	... <	-1.41	... <	0.14	...

NOTE—Abundances are determined differentially using G 64–12 as a reference, and the uncertainties represent internal precision only.

^a $[X/Fe]$ is calculated using the solar abundance from [Asplund et al. \(2009\)](#).

5. DISCUSSION

5.1. Lithium Abundances of Extremely Metal-Poor stars

The Li abundances of our program sample are shown in Figures 5 and 6, together with stars from the literature. Previous Li measurements and data selection for the plotting are summarized in the Appendix. Our sample efficiently covers lower metallicities than most previous samples, $[Fe/H] < -3.5$. The average of the Li abundances below $[Fe/H] = -3.5$ in our sample is $\langle A(Li) \rangle = 1.90$, with a scatter of 0.10 dex, which does not represent a dispersion larger than can be accounted for by the errors of determination.

One possible concern for interpretation of our results is the different choice of temperature scale. Adopting 100 K hotter temperatures makes the metallicities 0.08 dex higher, and $A(Li)$ 0.08 dex higher. A higher temperature scale by ~ 300 K would bring the lithium abundances of our sample onto the Spite Plateau level. However, our analysis is carried out differentially to G 64–12, for which our analysis of its Li abundance place it on the Spite Plateau. In addition, SDSS J1424+5615, at $[Fe/H] = -3.10$, was analysed by the same procedure and has a Li abundance close to the plateau value. Considering the Li abundances of G 64–12 and SDSS J1424+5615, the overall temperature scale of our analysis is unlikely to be the reason for the low Li abundances among the stars with lower metallicity.

We conclude that all stars in our sample with $[Fe/H] < -3.5$ have lower Li abundance than the Spite Plateau, by ~ 0.3 dex, with no scatter within the measurements

errors. Hereafter we combine our results with the literature sample.

As found from our sample, no star in the literature has comparable Li abundance to the Spite Plateau below $[Fe/H] \lesssim -3.5$, except for the primary of the double-lined binary system CS 22876–032. Thus, Li abundances appear to be uniformly low at extremely low metallicity. Our sample fills in the gap between Li measurements for stars around $[Fe/H] \sim -3.5$ and the two previously studied unevolved objects below $[Fe/H] < -4.0$, LAMOST J1253+0753 ($[Fe/H] = -4.02$, $A(Li) = 1.80$; [Li et al. 2015](#)) and HE 0233–0343 ($[Fe/H] = -4.7$, $A(Li) = 1.77$; [Hansen et al. 2014](#)). The Li abundances are almost flat or slightly decreasing from $[Fe/H] \sim -3.5$ to -4.5 , with relatively small scatter. Below $[Fe/H] \lesssim -5.0$, the observed Li abundances could show a sharp drop, though there are only two stars that provide useful data. Note that the possible existence of a “dual plateau” with a separation of 0.1 dex are discussed for stars with $[Fe/H] \gtrsim -2.5$ and $[Fe/H] \lesssim -2.5$ by [Meléndez et al. \(2010\)](#). The newly found constancy in the present work is at lower metallicity by 1.0 dex and with larger deviation from the Spite Plateau.

The combination of atomic diffusion and turbulent mixing has been proposed as a means to explain the lower Li abundance for stars on the Spite Plateau compared to the predicted primordial Li abundance ([Richard et al. 2005](#); [Michaud et al. 2015](#)). The model has been only tuned for $[Fe/H] = -2.3$ in [Richard et al. \(2005\)](#). The key parameter is the strength of the turbulent mixing, through which the model is adjusted. Small differences in this parameter can cause a large surface

Li abundance difference (see Fig. 3 in Richard et al. 2005). If this parameter has a metallicity dependence, this model might provide a solution.

Fu et al. (2015) suggested that all Li in the atmospheres of metal-poor stars is accreted *after* star formation; they attributed the low lithium abundances at $[\text{Fe}/\text{H}] < -2.5$ to weak accretion. The model needs fine tuning to reproduce the Spite Plateau, and it is not yet clear whether it can account for our finding that all stars below $[\text{Fe}/\text{H}] = -3.5$ have lower Li abundances, with a small scatter.

5.2. Chemical Inhomogeneity in the Early Universe

The early Universe is expected to be chemically inhomogeneous, since a small number of nucleosynthesis events can create large abundance fluctuations from one place to another; the observed scatter of the elemental abundances for EMP stars can be used to quantify this inhomogeneity. The variations in yields from supernovae explosions of the first stars (Nomoto et al. 2013; Tominaga et al. 2014) are primarily determined by differences in their explosion energies and masses.

We have carried out χ^2 tests to examine whether the observed scatter in $[\text{X}/\text{Fe}]$ ($A(\text{Li})$ for Li) is significant. The probability that stars having the same abundance exhibit a scatter only due to measurement errors is listed in Table 7. Stars without detection are excluded in this analysis. We find statistically significant scatter for $[\text{Na}/\text{Fe}]$, $[\text{Mg}/\text{Fe}]$, $[\text{Cr}/\text{Fe}]$, $[\text{Ti}/\text{Fe}]$, $[\text{Sr}/\text{Fe}]$, and $[\text{Ba}/\text{Fe}]$. On the other hand, $A(\text{Li})$, $[\text{Ca}/\text{Fe}]$ and $[\text{Sc}/\text{Fe}]$ do not exhibit significant scatter even at extremely low metallicity, although the number of stars with detection of Sc is small. Thus, Ca and Fe seem to be produced at almost a constant ratio irrespective of the progenitor. This ensures the effectiveness of searches for metal-poor stars using Ca lines. Since C is detected only in three of our program stars, it is excluded from this discussion.

The significant scatter observed for many elements indicate that the natal clouds for early generation stars are chemically inhomogeneous, reflecting variations in the yields of first stars and possible variations in mixing. However, the scatter in these elements is small compared to that predicted from the yields of supernovae explosions, considering the mass range of the progenitor (Kobayashi et al. 2006). The small scatter might indicate that the mini-halos hosting the early formation of EMP stars are also polluted by supernovae exploding in neighboring mini-halos (Jeon et al. 2017).

The abundance ratio $[\text{Na}/\text{Fe}]$ apparently exhibits a bimodal distribution (Figure 4). The Na abundances could be affected both by the adopted analysis technique and internal processes intrinsic to a given star.

For instance, large NLTE effects in the formation of Na I D lines have been predicted (Andrievsky et al. 2007). However, the NLTE effect is almost systematic within the narrow parameter range of our sample. Indeed, no significant difference in stellar parameters is found between the stars with high and low Na abundances. This stands in clear contrast to previous studies of EMP stars, which often include red giants having a wide range of stellar parameters compared to main-sequence turn-off stars. Another difficulty in the studies of red giants is that Na abundances could be affected by internal mixing during the evolution along the red giant branch. Therefore, it has been difficult to reach any conclusion about the Na abundance scatter from the sample including red giants. Our study on turn-off stars provides a unique sample to investigate the scatter and bimodal distribution of Na abundance at the lowest metallicity. Hence, the bimodal distribution of $[\text{Na}/\text{Fe}]$ in our result is regarded not as a result of analysis, but as a physical property of EMP stars.

In order to assess the origin of the observed bimodality, we examine possible connections between the Na abundances and those of other elements. First, the sample is divided into two groups at $[\text{Na}/\text{Fe}] = 0.0$. We compute the probability that both sub-samples have the same mean abundance, which is listed in the last column of Table 7. No significant difference is found for the abundances within the measurement errors. Even if the same test is made excluding SDSS J1424+5615, which has > 0.4 dex higher metallicity than rest of the stars, the results remain the same. Whereas correlations between $[\text{Na}/\text{Fe}]$ and $A(\text{Li})$ in globular clusters has been reported (Lind et al. 2009), we find no evidence for this in our sample.

Although the Na abundance may be related to a star's C abundance, as discussed in Section 4.2.1, the difficulty in deriving C abundances for the majority of our EMP turn-off stars prohibits a clear conclusion. The $[\text{Na}/\text{Fe}]$ bimodality and its association with C abundance has been already reported (e.g., Norris et al. 2013b). Note, however, that the difference in $[\text{Na}/\text{Fe}]$ between their two populations ($\Delta[\text{Na}/\text{Fe}] \sim 2.0$ dex) is much larger than ours ($\Delta[\text{Na}/\text{Fe}] \sim 0.8$ dex). The apparent $[\text{Na}/\text{Fe}]$ bimodality should be confirmed and investigated in detail by studies of a larger sample of EMP turn-off stars.

5.3. Metallicity Distribution Function

We now consider the metallicity distribution function (MDF) of the full sample of Aoki et al. (2013), shown in Figure 7. For the eight stars re-analyzed in the present study, we replace the metallicities with the newly derived ones. Since Aoki et al. (2013) adopt stellar pa-

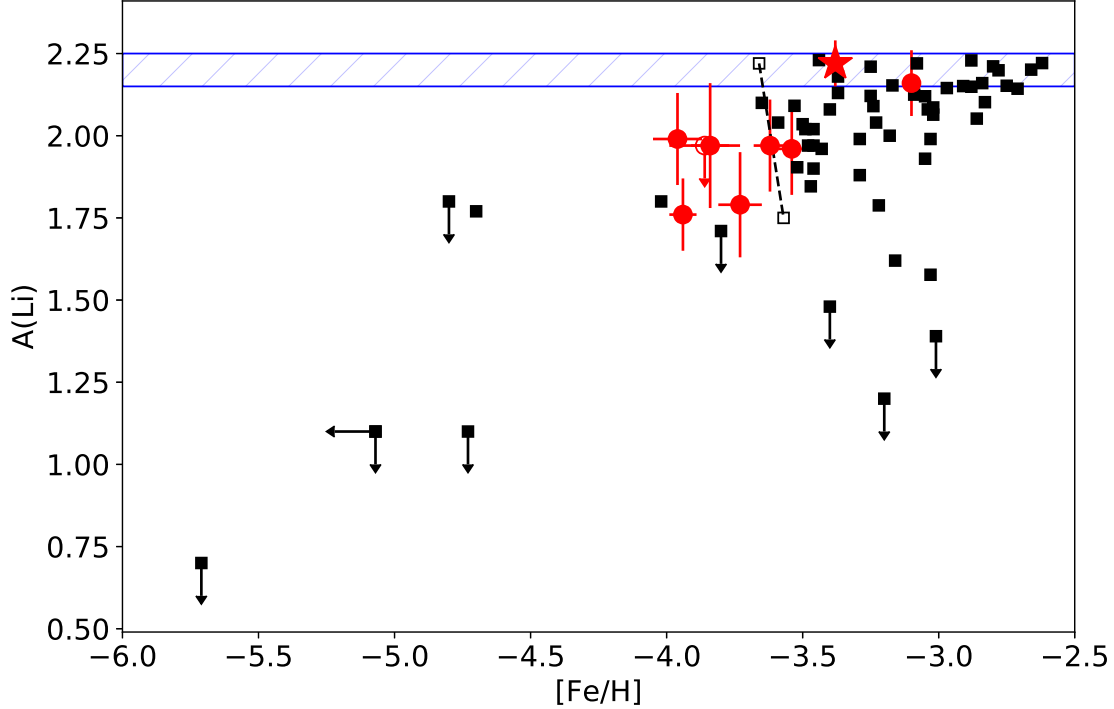


Figure 5. $A(\text{Li})$ as a function of $[\text{Fe}/\text{H}]$. Our sample is shown by red circles for the SDSS program stars and a star for G 64–12. Literature data are shown in black squares, compiled from Bonifacio et al. (2007); Frebel et al. (2008); Aoki et al. (2009); Sbordone et al. (2010); Caffau et al. (2011); Bonifacio et al. (2012, 2015); Li et al. (2015). A double-lined spectroscopic binary system, CS 22876–032, is shown by open squares with the individual Li abundances connected to each other (Norris et al. 2000; González Hernández et al. 2008). The blue hatched region indicates the Spite Plateau, $A(\text{Li}) = 2.2 \pm 0.1$.

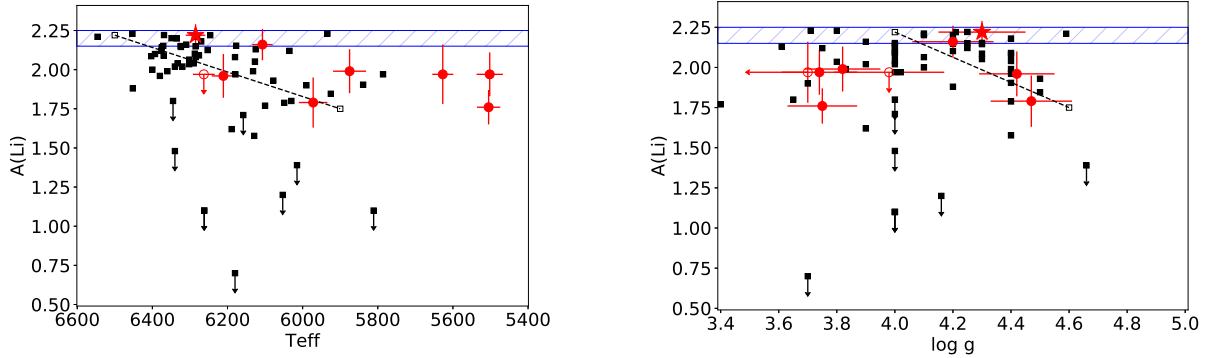


Figure 6. $A(\text{Li})$ as a function of T_{eff} and $\log g$. The symbols are the same as in Figure 5.

rameters from the SSPP, which derives higher T_{eff} than the present study, there is a difference in the metallicity scale between the two results. From a comparison of the stars in common between these studies (excepting SDSS J2309+2308 and SDSS J2005–1045), our metallicity scale is ~ 0.28 dex lower and the T_{eff} scale is ~ 300 K lower than that of Aoki et al. (2013). Since metallicity is lowered by ~ 0.08 dex when 100 K lower T_{eff} is adopted, the 0.28 dex offset is almost consistent

with the value expected from our ~ 350 K cooler T_{eff} than the SSPP. We take a 0.28 dex shift into account in the replacement and generate the MDF on the scale of the present study. The optimal bin size is determined following Shimazaki & Shinomoto (2007), 0.10 dex. We also create generalized histograms with a Gaussian function whose σ is 0.10 dex. No significant spurious features are seen in the distribution. Note that our MDF above

Table 7. Scatter in $[X/Fe]$ (or $A(Li)$ for Li) and Probabilities

Element	Std. Deviation ^a	p_{Scatter} ^b	$p_{\text{Na-group}}$ ^c
$[Fe/H]$	0.33	0.00	0.14
Li I	0.15	0.21	0.07
Na I	0.48	0.00	0.00
Mg I	0.30	0.00	0.21
Ca I	0.15	0.16	0.19
Cr I	0.26	0.00	...
Sc II	0.16	0.06	...
Ti II	0.26	0.00	0.65
Sr II	0.28	0.00	...
Ba II	0.79	0.00	...

^aStars without detection are excluded.

^bThe probabilities that elemental abundances are the same for the whole sample (see Text).

^cThe probabilities of Na-rich and Na-poor groups having the same abundances.

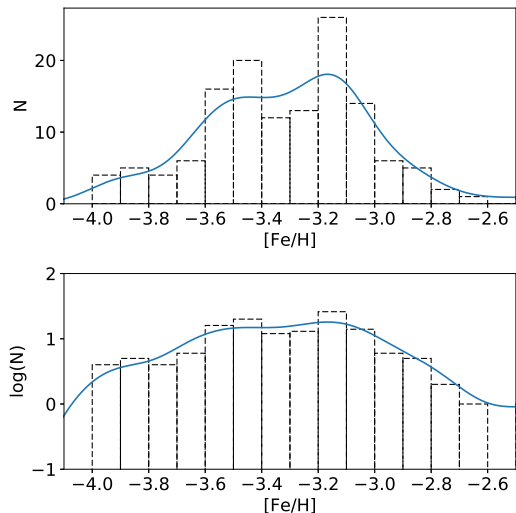


Figure 7. The MDF of the full sample of SDSS main-sequence turnoff stars from Aoki et al. (2013), on a linear scale (upper panel) and on a logarithmic scale (lower panel). The solid blue lines are generalized histograms with a Gaussian convolution with $\sigma = 0.10$ dex. The metallicity of Aoki et al. (2013) is shifted by 0.28 dex to match our metallicity scale.

$[Fe/H] \sim -3.4$ appears to be significantly affected by the incompleteness of the target selection (Aoki 2012).

Schörck et al. (2009) and Li et al. (2010) reported a cut-off in the MDFs for giants and turn-off stars among candidate metal-poor stars from the Hamburg/ESO survey (Christlieb et al. 2008), at around $[Fe/H] \sim -3.5$. We do not find evidence for such a cut-off in the MDF of our sample down to $[Fe/H] \sim -4.0$, consistent with Yong et al. (2013). If the 0.28 dex metallicity correction is not applied, the existence of the tail is still clear.

5.4. Extremely Metal-Poor CEMP-s stars

SDSS J1036+1212 is one of the lowest metallicity CEMP-s stars known. Although Behara et al. (2010) reported on a detailed abundance pattern for SDSS J1036+1212, we could not detect as many elements as they reported. We obtained the VLT/UVES spectrum of SDSS J1036+1212 used by Behara et al. (2010) for their abundance analysis from the ESO archive. However, we could not reproduce their reported detection of Eu. Hence, we here discuss this object based solely on the abundance results obtained by the present work.

SDSS J2309+2308 exhibits an excess of Ba, and is another candidate CEMP-s star, although only a weak upper limit on its C abundance is determined by our study.

CEMP-s stars are generally considered to have experienced mass transfer from an AGB companion in which large amounts of C and s-process elements, including Ba, are synthesized. The reported high binary frequency among such stars supports this scenario (Starkenburger et al. 2014; Hansen et al. 2016). Although neither of these two stars exhibited a radial velocity variation between our observations and Aoki et al. (2013), the radial velocity of SDSS J1036+1212 in our work is $\sim 14 \text{ km s}^{-1}$ larger than Behara et al. (2010), suggesting the likely binarity of this object.

Although two extremely metal-poor CEMP-s candidates are found in our sample, there is a lack of such stars among the red giants shown as found Figure 8. Among the CEMP-s stars with $[Fe/H] < -3.0$, almost all stars with $[Ba/Fe] > +1.0$ are main-sequence stars. The lack of CEMP-s red giants in $[Fe/H] < -3.0$ may be related to the first dredge-up that occurs at the beginning of the red giant phase. First dredge-up dilutes the surface material of a star to the inner regions. If the over-abundance of Ba is provided by mass transfer from a companion star to the stellar surface, first dredge-up significantly reduces the surface Ba abundance. Such dilution is effective only when i) the transferred mass is small compared to the dredged-up mass, and ii) transferred material is not mixed with the interior during main-sequence stage. Since the dredged-up mass is large ($\sim 50\%$ of the stellar mass), the first condition is gener-

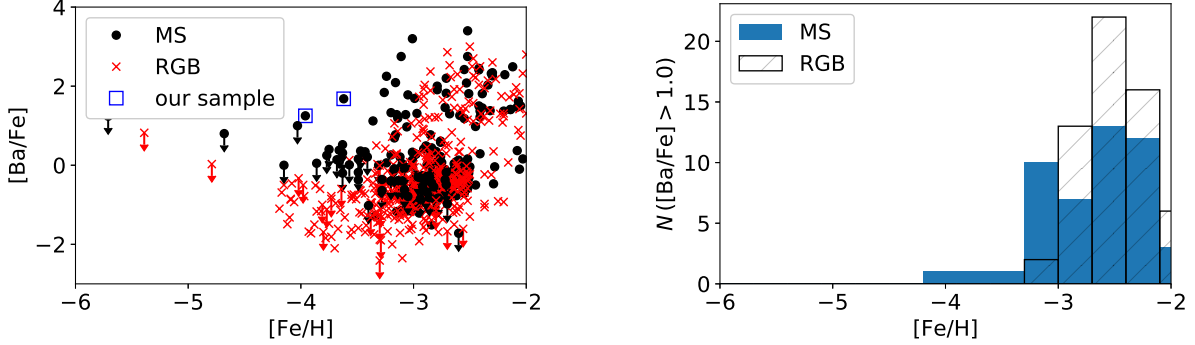


Figure 8. The distribution of $[\text{Ba}/\text{Fe}]$, as a function of $[\text{Fe}/\text{H}]$, for stars selected from the SAGA database (Suda et al. 2008) and the two possible CEMP- s stars in our sample. Classifications of main-sequence stars (MS; black dots) and red giants (RGB; red crosses) are those provided by SAGA. *Left:* $[\text{Ba}/\text{Fe}]$ as a function of $[\text{Fe}/\text{H}]$. *Right:* Metallicity distribution of Ba-rich stars ($[\text{Ba}/\text{Fe}] > +1.0$).

ally satisfied (see also Masseron et al. 2012). Therefore, the existence of extremely metal-poor CEMP- s turn-off stars is a potential constraint on the efficiency of mixing processes during the main-sequence phase, such as thermohaline mixing (Stancliffe et al. 2007). The reason for the lack of CEMP- s red giants at only extremely low metallicity might be that the efficiency of the operation of the s -process is low in this regime.

Note that the above discussion using the SAGA database can be affected by sample selection, since some past studies focus on red giants while others focus on turn-off stars. For example, Jacobson et al. (2015) have constructed a sample of metal-poor stars on the red giant branch using photometric estimates of metallicity, and reported a lack of extremely carbon-rich objects. Jacobson et al. (2015) suspected that the use of photometric selection of metal-poor stars may have resulted in a bias against such objects. On the other hand, some previous studies focused on turn-off CEMP stars (e.g., Aoki et al. 2008). To obtain a clear conclusion regarding the lack of CEMP- s red giants at $[\text{Fe}/\text{H}] < -3$, we require a larger sample of EMP stars including both red giants and turn-off stars.

6. SUMMARY

We analyze eight unevolved EMP stars for which Aoki et al. (2013) have previously estimated abundances from snapshot spectroscopy. Based on newly obtained high-resolution, high- S/N spectra, we first compare different methods to derive stellar parameters. Analysis of Balmer-line profiles derive consistent T_{eff} estimates with an Fe-lines analysis and $V - K_s$ color-based temperature estimates. The surface gravity estimates obtained from the Balmer-line analysis are also consistent with those from the Fe-lines analysis and from Gaia parallaxes. In

contrast, the SSPP procedure results in higher T_{eff} estimates than the Balmer-line analysis for EMP stars.

We carry out a differential abundance analysis, with G 64-12 as a reference, adopting the parameters obtained by Balmer-line analysis. The use of the reference star should cancel out NLTE/3D effects and atomic data uncertainties. We obtain the following results:

1. Seven of the eight stars have $[\text{Fe}/\text{H}] < -3.5$ and all have $T_{\text{eff}} > 5500$ K.
2. Lithium abundances of all seven stars below $[\text{Fe}/\text{H}] = -3.5$ are lower than the Spite Plateau, without significant scatter. This result could provide a constraint on proposed Li-depletion mechanisms.
3. We found significant scatter in $[\text{Na}/\text{Fe}]$, $[\text{Mg}/\text{Fe}]$, $[\text{Cr}/\text{Fe}]$, $[\text{Ti}/\text{Fe}]$, $[\text{Sr}/\text{Fe}]$ and $[\text{Ba}/\text{Fe}]$. On the other hand, the scatter in $A(\text{Li})$, $[\text{Sc}/\text{Fe}]$, and $[\text{Ca}/\text{Fe}]$ are not significant. The observed bimodality in $[\text{Na}/\text{Fe}]$, with a separation of 0.8 dex, requires explanation; further confirmation and detailed investigation with larger samples is desired.
4. We confirm the most metal-poor CEMP- s star yet known and identify another CEMP- s candidate with $[\text{Fe}/\text{H}] \sim -4.0$. From literature data, a lack of CEMP- s red giants with $[\text{Fe}/\text{H}] < -3.0$ is seen. Their absence may be due to the combined effect of metallicity dependence of s -process efficiency and dilution caused by first dredge-up.

From the point of the comparison between observations and suggested Li-depletion models, atomic diffusion with turbulent mixing (e.g., Richard et al. 2005) should be investigated for a wider range of parameter

space, especially toward lower metallicity. More quantitative evaluation is needed for other models, such as Li depletion due to astration by first stars or Li depletion in the pre-main sequence phase. More precise stellar parameters, in particular evolutionary phase and mass, and more precise abundances are clearly desired. Improved $\log g$ estimates which will be provided by Gaia parallaxes should result in significant progress. It is also desired to increase the sample size of EMP main-sequence turn-off stars.

We thank H. Ito for the data reduction and observation. The authors are thankful to anonymous referee for the comments. This work is based in part on data collected at Subaru Telescope and obtained from

the SMOKA, which is operated by the Astronomy Data Center, National Astronomical Observatory of Japan. WA was supported by JSPS KAKENHI Grant Numbers JP16H02168. This work received partial support from PHY 14–30152; Physics Frontier Center/JINA Center for the Evolution of the Elements (JINA-CEE), awarded by the US National Science Foundation. This work was supported in part by the Center for the Promotion of Integrated Sciences (CPIS) of SOKENDAI. Y.S.L. acknowledges partial support from the National Research Foundation of Korea to the Center for Galaxy Evolution Research and Basic Science Research Program through the National Research Foundation of Korea (NRF) funded by the Ministry of Science, ICT and Future Planning (NRF-2015R1C1A1A02036658).

APPENDIX

A. ADOPTED VALUES IN THE TABLES

Previous measurements of Li abundances for metal-poor stars are listed in Table 8. We exclude stars with $T_{\text{eff}} < 5500$ K or $[\text{Fe}/\text{H}] > -2.5$. There are overlaps in the samples among [Aoki et al. \(2009\)](#), [Sbordone et al. \(2010\)](#) and [Bonifacio et al. \(2007\)](#), for which we gave priority in this order. Each star appears once in each figure, though we plot both of our results and the results of [Aoki et al. \(2009\)](#) for G 64–12.

Table 8. Li Abundance Measurements from Previous Studies and in this Work

Object	T_{eff}	$\log g$	$[\text{Fe}/\text{H}]$	$A(\text{Li})$	Reference
CD -24°17504	6180	4.4	-3.40	2.08	Aoki et al. (2009)
BS 16023-046	6324	4.30	-2.97	2.145	Sbordone et al. (2010)
	6364	4.50	-2.97	2.18	Bonifacio et al. (2007)
BS 16545-089	6320	3.9	-3.49	2.02	Aoki et al. (2009)
BS 16968-061	6035	3.75	-3.05	2.12	Bonifacio et al. (2007)
BS 17570-063	6078	4.50	-3.05	1.930	Sbordone et al. (2010)
	6242	4.75	-2.92	2.05	Bonifacio et al. (2007)
BS 17572-100	6371	4.00	-2.75	2.152	Sbordone et al. (2010)
CS 22177-009	6177	4.30	-3.17	2.153	Sbordone et al. (2010)
	6257	4.50	-3.10	2.21	Bonifacio et al. (2007)
CS 22188-033	6129	4.40	-3.03	1.577	Sbordone et al. (2010)
CS 22876-032A	6500	4.0	-3.66	2.22	González Hernández et al. (2008)
CS 22876-032B	5900	4.6	-3.57	1.75	González Hernández et al. (2008)
CS 22888-031	5925	4.50	-3.47	1.846	Sbordone et al. (2010)
	6151	5.00	-3.30	2.01	Bonifacio et al. (2007)
CS 22948-093	6380	4.4	-3.43	1.96	Aoki et al. (2009)

Table 8 continued

Table 8 (*continued*)

Object	T_{eff}	$\log g$	[Fe/H]	$A(\text{Li})$	Reference
	6356	4.25	-3.30	1.94	Bonifacio et al. (2007)
	6365	4.25	-3.31	1.935	Sbordone et al. (2010)
CS 22950-173	6335	4.20	-2.78	2.199	Sbordone et al. (2010)
CS 22953-037	6325	4.25	-2.91	2.151	Sbordone et al. (2010)
	6364	4.25	-2.89	2.16	Bonifacio et al. (2007)
CS 22965-054	6310	3.9	-2.84	2.16	Aoki et al. (2009)
	6089	3.75	-3.04	2.03	Bonifacio et al. (2007)
	6245	4.00	-2.90	2.161	Sbordone et al. (2010)
CS 22966-011	6049	4.40	-3.22	1.788	Sbordone et al. (2010)
	6204	4.75	-3.07	1.90	Bonifacio et al. (2007)
CS 29491-084	6285	4.00	-3.04	2.080	Sbordone et al. (2010)
	6318	4.00	-2.70	2.18	Bonifacio et al. (2007)
CS 29499-060	6349	4.10	-2.66	2.201	Sbordone et al. (2010)
CS 29506-007	6285	4.20	-2.88	2.149	Sbordone et al. (2010)
	6273	4.00	-2.91	2.15	Bonifacio et al. (2007)
CS 29506-090	6287	4.20	-2.83	2.102	Sbordone et al. (2010)
	6303	4.25	-2.83	2.12	Bonifacio et al. (2007)
CS 29514-007	6281	4.10	-2.80	2.211	Sbordone et al. (2010)
CS 29516-028	5839	4.40	-3.52	1.904	Sbordone et al. (2010)
CS 29518-020	6127	4.30	-2.86	2.052	Sbordone et al. (2010)
	6242	4.50	-2.77	2.14	Bonifacio et al. (2007)
CS 29518-043	6376	4.25	-3.25	2.121	Sbordone et al. (2010)
	6432	4.25	-3.20	2.17	Bonifacio et al. (2007)
CS 29527-015	6276	4.00	-3.53	2.091	Sbordone et al. (2010)
	6242	4.00	-3.55	2.07	Bonifacio et al. (2007)
CS 30301-024	6375	4.00	-2.71	2.143	Sbordone et al. (2010)
	6334	4.00	-2.75	2.12	Bonifacio et al. (2007)
CS 30302-145	6403	4.30	-3.02	2.086	Sbordone et al. (2010)
CS 30339-069	6253	4.00	-3.09	2.125	Sbordone et al. (2010)
	6242	4.00	-3.08	2.13	Bonifacio et al. (2007)
CS 30344-070	6302	4.10	-3.02	2.064	Sbordone et al. (2010)
CS 31061-032	6369	4.25	-2.62	2.221	Sbordone et al. (2010)
	6409	4.25	-2.58	2.25	Bonifacio et al. (2007)
G 64-12	6270	4.4	-3.37	2.18	Aoki et al. (2009)
G 64-12	6285	4.30	-3.38	2.22	This work
G 64-37	6290	4.4	-3.23	2.04	Aoki et al. (2009)
HE 0148-2611	6400	4.10	-3.18	2.000	Sbordone et al. (2010)
HE 0233-0343	6100	3.4	-4.7	1.77	Hansen et al. (2014)

Table 8 *continued*

Table 8 (continued)

Object	T_{eff}	$\log g$	[Fe/H]	$A(\text{Li})$	Reference
HE 1148–0037	5990	3.7	-3.46	1.90	Aoki et al. (2009)
HE 1327–2326	6180	3.7	-5.71	<0.70	Frebel et al. (2008)
HE 1413–1954	6302	3.80	-3.50	2.035	Sbordone et al. (2010)
LAMOST J1253+0753	6030	3.65	-4.02	1.80	Li et al. (2015)
LP 815–43	6453	3.80	-2.88	2.229	Sbordone et al. (2010)
SDSS J002113–005005	6546	4.59	-3.25	2.21	Bonifacio et al. (2012)
SDSS J002749+140418	6125	3.61	-3.37	2.13	Bonifacio et al. (2012)
SDSS J0040+16	6360	4.4	-3.29	1.99	Aoki et al. (2009)
SDSS J0120–1001	5627	<3.70	-3.84	1.97	This work
SDSS J0212+0137	6333	4.0	-3.59	2.04	Bonifacio et al. (2015)
SDSS J031745+002304	5786	4.02	-3.46	1.97	Bonifacio et al. (2012)
SDSS J082118+181931	6158	4.00	-3.80	<1.71	Bonifacio et al. (2012)
SDSS J082521+040334	6340	4.00	-3.46	2.02	Bonifacio et al. (2012)
SDSS J090733+024608	5934	3.71	-3.44	2.23	Bonifacio et al. (2012)
SDSS J102915+172927	5811	4.0	-4.73	<1.1	Caffau et al. (2011)
SDSS J1033+40	6370	4.4	-3.24	2.09	Aoki et al. (2009)
SDSS J1035+0641	6262	4.0	<-5.07	<1.1	Bonifacio et al. (2015)
SDSS J1036+1212	5502	3.74	-3.62	1.97	This work
SDSS J113528+010848	6132	3.83	-3.03	1.99	Bonifacio et al. (2012)
SDSS J1137+2553	6310	3.2	-2.70	2.26	Bonifacio et al. (2015)
SDSS J122935+262445	6452	4.20	-3.29	1.88	Bonifacio et al. (2012)
SDSS J130017+263238	6393	4.00	-3.65	2.10	Bonifacio et al. (2012)
SDSS J1424+5615	6107	4.20	-3.10	2.16	This work
SDSS J143632+091831	6340	4.00	-3.40	<1.48	Bonifacio et al. (2012)
SDSS J144640+124917	6189	3.90	-3.16	1.62	Bonifacio et al. (2012)
SDSS J1522+3055	5505	3.75	-3.94	1.76	This work
SDSS J154246+054426	6179	4.00	-3.48	1.97	Bonifacio et al. (2012)
SDSS J1640+3709	6211	4.42	-3.54	1.96	This work
SDSS J1742+2531	6345	4.0	-4.80	<1.8	Bonifacio et al. (2015)
SDSS J2005–1045	6263	3.98	-3.86	<1.97	This work
SDSS J223143–094834	6053	4.16	-3.20	<1.20	Bonifacio et al. (2012)
SDSS J230814–085526	6015	4.66	-3.01	<1.39	Bonifacio et al. (2012)
SDSS J2309+2308	5875	3.82	-3.96	1.99	This work
SDSS J233113–010933	6246	4.21	-3.08	2.22	Bonifacio et al. (2012)
SDSS J2349+3832	5972	4.47	-3.73	1.79	This work

NOTE—The first reference for each star in this table is adopted in the plots (Figures 5, 6).

REFERENCES

Aldenius, M., Tanner, J. D., Johansson, S., Lundberg, H.,
& Ryan, S. G. 2007, A&A, 461, 767

Allende Prieto, C., Sivarani, T., Beers, T. C., et al. 2008,
AJ, 136, 2070

- Andrievsky, S. M., Spite, M., Korotin, S. A., et al. 2007, *A&A*, 464, 1081
- Aoki, W. 2012, in *Astronomical Society of the Pacific Conference Series*, Vol. 458, *Galactic Archaeology: Near-Field Cosmology and the Formation of the Milky Way*, ed. W. Aoki, M. Ishigaki, T. Suda, T. Tsujimoto, & N. Arimoto, 55
- Aoki, W., Barklem, P. S., Beers, T. C., et al. 2009, *ApJ*, 698, 1803
- Aoki, W., Frebel, A., Christlieb, N., et al. 2006, *ApJ*, 639, 897
- Aoki, W., Beers, T. C., Sivarani, T., et al. 2008, *ApJ*, 678, 1351
- Aoki, W., Beers, T. C., Lee, Y. S., et al. 2013, *AJ*, 145, 13
- Asplund, M. 2005, *ARA&A*, 43, 481
- Asplund, M., Grevesse, N., Sauval, A. J., & Scott, P. 2009, *ARA&A*, 47, 481
- Baba, H., Yasuda, N., Ichikawa, S.-I., et al. 2002, in *Astronomical Society of the Pacific Conference Series*, Vol. 281, *Astronomical Data Analysis Software and Systems XI*, ed. D. A. Bohlender, D. Durand, & T. H. Handley, 298
- Bard, A., Kock, A., & Kock, M. 1991, *A&A*, 248, 315
- Barklem, P. S., Stempels, H. C., Allende Prieto, C., et al. 2002, *A&A*, 385, 951
- Beers, T. C., & Christlieb, N. 2005, *ARA&A*, 43, 531
- Behara, N. T., Bonifacio, P., Ludwig, H.-G., et al. 2010, *A&A*, 513, A72
- Bonifacio, P., Sbordone, L., Caffau, E., et al. 2012, *A&A*, 542, A87
- Bonifacio, P., Molaro, P., Sivarani, T., et al. 2007, *A&A*, 462, 851
- Bonifacio, P., Caffau, E., Spite, M., et al. 2015, *A&A*, 579, A28
- Caffau, E., Bonifacio, P., François, P., et al. 2011, *Nature*, 477, 67
- Casagrande, L., Ramírez, I., Meléndez, J., Bessell, M., & Asplund, M. 2010, *A&A*, 512, A54
- Castelli, F., & Kurucz, R. L. 2003, in *IAU Symposium*, Vol. 210, *Modelling of Stellar Atmospheres*, ed. N. Piskunov, W. W. Weiss, & D. F. Gray, A20
- Christlieb, N., Schörck, T., Frebel, A., et al. 2008, *A&A*, 484, 721
- Coc, A., Vangioni-Flam, E., Descouvemont, P., Adahchour, A., & Angulo, C. 2004, *ApJ*, 600, 544
- Cutri, R. M., Skrutskie, M. F., van Dyk, S., et al. 2003, *VizieR Online Data Catalog*, 2246
- Cybert, R. H., Fields, B. D., Olive, K. A., & Yeh, T.-H. 2016, *Reviews of Modern Physics*, 88, 015004
- Frebel, A., Collet, R., Eriksson, K., Christlieb, N., & Aoki, W. 2008, *ApJ*, 684, 588
- Froese Fischer, C. 1975, *Canadian Journal of Physics*, 53, 184, (FFa)
- Fu, X., Bressan, A., Molaro, P., & Marigo, P. 2015, *MNRAS*, 452, 3256
- Fuhr, J. R., Martin, G. A., & Wiese, W. L. 1988, *Journal of Physical and Chemical Reference Data*, 17
- Gaia Collaboration, Brown, A. G. A., Vallenari, A., et al. 2016a, *A&A*, 595, A2
- Gaia Collaboration, Prusti, T., de Bruijne, J. H. J., et al. 2016b, *A&A*, 595, A1
- González Hernández, J. I., Bonifacio, P., Ludwig, H.-G., et al. 2008, *A&A*, 480, 233
- Grevesse, N., Biemont, E., Lowe, R. M., & Hannaford, P. 1981, in *Liege International Astrophysical Colloquia*, Vol. 23, *Liege International Astrophysical Colloquia*, 211–222
- Grevesse, N., Blackwell, D. E., & Petford, A. D. 1989, *A&A*, 208, 157
- Grevesse, N., Scott, P., Asplund, M., & Sauval, A. J. 2015, *A&A*, 573, A27
- Hampel, M., Stancliffe, R. J., Lugaro, M., & Meyer, B. S. 2016, *ApJ*, 831, 171
- Hansen, T., Hansen, C. J., Christlieb, N., et al. 2014, *ApJ*, 787, 162
- Hansen, T. T., Andersen, J., Nordström, B., et al. 2016, *A&A*, 588, A3
- Henden, A. A., Templeton, M., Terrell, D., et al. 2016, *VizieR Online Data Catalog*, 2336
- Ivans, I. I., Simmerer, J., Sneden, C., et al. 2006, *ApJ*, 645, 613
- Jacobson, H. R., Keller, S., Frebel, A., et al. 2015, *ApJ*, 807, 171
- Jeon, M., Besla, G., & Bromm, V. 2017, *ArXiv e-prints*, arXiv:1702.07355
- Jordi, K., Grebel, E. K., & Ammon, K. 2006, *A&A*, 460, 339
- Kim, Y.-C., Demarque, P., Yi, S. K., & Alexander, D. R. 2002, *ApJS*, 143, 499
- Kobayashi, C., Umeda, H., Nomoto, K., Tominaga, N., & Ohkubo, T. 2006, *ApJ*, 653, 1145
- Lawler, J. E., & Dakin, J. T. 1989, *Journal of the Optical Society of America B Optical Physics*, 6, 1457
- Lawler, J. E., Guzman, A., Wood, M. P., Sneden, C., & Cowan, J. J. 2013, *ApJS*, 205, 11
- Lee, Y. S., Beers, T. C., Sivarani, T., et al. 2008a, *AJ*, 136, 2022
- . 2008b, *AJ*, 136, 2050
- Li, H., Aoki, W., Zhao, G., et al. 2015, *PASJ*, 67, 84

- Li, H. N., Christlieb, N., Schörck, T., et al. 2010, *A&A*, 521, A10
- Lind, K., Asplund, M., & Barklem, P. S. 2009, *A&A*, 503, 541
- Lind, K., Bergemann, M., & Asplund, M. 2012, *MNRAS*, 427, 50
- Madau, P., & Dickinson, M. 2014, *ARA&A*, 52, 415
- Martin, G. A., Fuhr, J. R., & Wiese, W. L. 1988, Atomic transition probabilities. Scandium through Manganese
- Masseron, T., Johnson, J. A., Lucatello, S., et al. 2012, *ApJ*, 751, 14
- Masseron, T., Plez, B., Van Eck, S., et al. 2014, *A&A*, 571, A47
- Matsuno, T., Aoki, W., Suda, T., & Li, H. 2017, *PASJ*, 69, 24
- Meléndez, J., & Barbuy, B. 2009, *A&A*, 497, 611
- Meléndez, J., Casagrande, L., Ramírez, I., Asplund, M., & Schuster, W. J. 2010, *A&A*, 515, L3
- Michaud, G., Alecian, G., & Richer, J. 2015, Atomic Diffusion in Stars (Springer International Publishing), doi:10.1007/978-3-319-19854-5
- Moity, J. 1983, *A&AS*, 52, 37
- Morton, D. C. 1991, *ApJS*, 77, 119
- Nissen, P. E., Akerman, C., Asplund, M., et al. 2007, *A&A*, 469, 319
- Noguchi, K., Aoki, W., Kawanomoto, S., et al. 2002, *PASJ*, 54, 855
- Nomoto, K., Kobayashi, C., & Tominaga, N. 2013, *ARA&A*, 51, 457
- Norris, J. E., Beers, T. C., & Ryan, S. G. 2000, *ApJ*, 540, 456
- Norris, J. E., Bessell, M. S., Yong, D., et al. 2013a, *ApJ*, 762, 25
- Norris, J. E., Yong, D., Bessell, M. S., et al. 2013b, *ApJ*, 762, 28
- O'Brian, T. R., Wickliffe, M. E., Lawler, J. E., Whaling, W., & Brault, J. W. 1991, *Journal of the Optical Society of America B Optical Physics*, 8, 1185
- Piau, L., Beers, T. C., Balsara, D. S., et al. 2006, *ApJ*, 653, 300
- Pickering, J. C., Thorne, A. P., & Perez, R. 2001, *ApJS*, 132, 403
- Pinnington, E. H., Berends, R. W., & Lumsden, M. 1995, *Journal of Physics B Atomic Molecular Physics*, 28, 2095
- Piskunov, N. E., Kupka, F., Ryabchikova, T. A., Weiss, W. W., & Jeffery, C. S. 1995, *A&AS*, 112, 525
- Placco, V. M., Beers, T. C., Reggiani, H., & Meléndez, J. 2016, *ApJL*, 829, L24
- Planck Collaboration, Adam, R., Ade, P. A. R., et al. 2016, *A&A*, 594, A1
- Reggiani, H., Meléndez, J., Yong, D., Ramírez, I., & Asplund, M. 2016, *A&A*, 586, A67
- Richard, O., Michaud, G., & Richer, J. 2005, *ApJ*, 619, 538
- Ryabchikova, T. A., Hill, G. M., Landstreet, J. D., Piskunov, N., & Sigut, T. A. A. 1994, *MNRAS*, 267, 697
- Ryan, S. G., Beers, T. C., Deliyannis, C. P., & Thorburn, J. A. 1996, *ApJ*, 458, 543
- Ryan, S. G., Norris, J. E., & Beers, T. C. 1999, *ApJ*, 523, 654
- Sbordone, L., Bonifacio, P., Caffau, E., et al. 2010, *A&A*, 522, A26
- Schlafly, E. F., & Finkbeiner, D. P. 2011, *ApJ*, 737, 103
- Schörck, T., Christlieb, N., Cohen, J. G., et al. 2009, *A&A*, 507, 817
- Shimazaki, H., & Shinomoto, S. 2007, *Neural Computation*, 19, 1503
- Smith, G., & Raggett, D. S. J. 1981, *Journal of Physics B Atomic Molecular Physics*, 14, 4015
- Smith, V. V., Lambert, D. L., & Nissen, P. E. 1998, *ApJ*, 506, 405
- Sobeck, J. S., Lawler, J. E., & Sneden, C. 2007, *ApJ*, 667, 1267
- Spite, F., & Spite, M. 1982a, *A&A*, 115, 357
- Spite, M., & Spite, F. 1982b, *Nature*, 297, 483
- Spite, M., Cayrel, R., Hill, V., et al. 2006, *A&A*, 455, 291
- Stancliffe, R. J., Glebbeek, E., Izzard, R. G., & Pols, O. R. 2007, *A&A*, 464, L57
- Starkenburger, E., Shetrone, M. D., McConnachie, A. W., & Venn, K. A. 2014, *MNRAS*, 441, 1217
- Suda, T., Yamada, S., Katsuta, Y., et al. 2011, *MNRAS*, 412, 843
- Suda, T., Katsuta, Y., Yamada, S., et al. 2008, *PASJ*, 60, 1159
- Tominaga, N., Iwamoto, N., & Nomoto, K. 2014, *ApJ*, 785, 98
- Wiese, W. L., & Martin, G. A. 1980, Wavelengths and transition probabilities for atoms and atomic ions: Part 2. Transition probabilities
- Wood, M. P., Lawler, J. E., Sneden, C., & Cowan, J. J. 2013, *ApJS*, 208, 27
- Yamada, S., Suda, T., Komiya, Y., Aoki, W., & Fujimoto, M. Y. 2013, *MNRAS*, 436, 1362
- Yanny, B., Rockosi, C., Newberg, H. J., et al. 2009, *AJ*, 137, 4377
- Yong, D., Norris, J. E., Bessell, M. S., et al. 2013, *ApJ*, 762, 27
- York, D. G., Adelman, J., Anderson, Jr., J. E., et al. 2000, *AJ*, 120, 1579